

Antisite disorder induced spin-glass and exchange bias phenomena in double perovskites



**Thesis submitted in partial fulfilment for the Award of Degree
DOCTOR OF PHILOSOPHY**

by
RAMAN HISSARIYA

**SCHOOL OF MATERIALS SCIENCE AND TECHNOLOGY
INDIAN INSTITUTE OF TECHNOLOGY (IIT)
VARANASI - 221 005
INDIA**

ROLL NUMBER
18111009

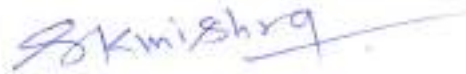
YEAR OF SUBMISSION
2023

Dedicated to my parents, daughter (DIVA) and the whole family that always encouraged me to follow my dreams.

Certificate

It is certified that the work contained in the thesis titled "**Antisite disorder induced spin-glass and exchange bias phenomena in double perovskites**" by Mr. Raman Hissariya, Roll Number **18111009**, has been carried out under my supervision and that this work has not been submitted elsewhere for a degree.

It is further certified that the student has fulfilled all the requirements of Comprehensive Examination, Candidacy and SOTA for the award of Ph.D. Degree.



Supervisor

Dr. Shrawan Kumar Mishra

School of Materials Science & Technology

IIT (BHU), Varanasi-221005

Assistant Professor/सहायक-आचार्य

School of Materials Science & Technology, Indian Institute of Technology (BHU), Varanasi

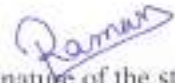
संस्थान सूक्ष्मदर्शन विभाग, भारतीय प्रौद्योगिकी संस्थान

Varanasi, India

Declaration

I, **Raman Hissariya**, certify that the work embodied in this thesis is my own bona-fide work and carried out by me under the supervision of **Dr. Shrawan Kumar Mishra** from **July 2018 to June 2023** at the **School of Materials Science & Technology**, Indian Institute of Technology (BHU), Varanasi. The matter embodied in this thesis has not been submitted for the award of any other degree/diploma. I declare that I have faithfully acknowledged and given credits to the research scholars/scientists wherever their works have been cited in my work in this thesis. I further declare that I have not willfully copied any others' work, paragraphs, text, data, results, etc., reported in journals, books, magazines, reports dissertations, theses, etc., or available at websites and have not included them in this thesis and have not cited as my own work.

Date: 16.06.2023
Place: Varanasi


Signature of the student
(Raman Hissariya)

Certificate by the Supervisor

It is certified that the above statement made by the student is correct to the best of my knowledge.


Dr. Shrawan Kumar Mishra

Assistant Professor
School of Materials Science & Technology
IIT (BHU), Varanasi
(Banaras Hindu University), Varanasi



Coordinator

School of Materials Science & Technology

IIT (BHU), Varanasi

Coordinator/समन्वयक

School of Materials Science & Technology/पर्याप्त विज्ञान एवं प्रौद्योगिकी स्कूल

Indian Institute of Technology/भारतीय प्रौद्योगिकी संस्थान

(Banaras Hindu University), Varanasi/काशी हिन्दू विश्वविद्यालय, वाराणसी

Copyright Transfer Certificate


Title of the Thesis : **Antisite disorder induced spin-glass and exchange bias phenomena in double perovskites**

Name of the Student : **Raman Hissariya**

Copyright Transfer

The undersigned hereby assigns to the Indian Institute of Technology (BHU), Varanasi all rights under copyright that may exist in and for the above thesis submitted for the award of the **Doctor of Philosophy**.

Date: 16.06.2023
Place: Varanasi


Signature of the student
(Raman Hissariya)

Note: However, the author may reproduce or authorize others to reproduce material extracted verbatim from the thesis or derivative of the thesis for author's personal use provided that the source and the Institute's copyright notice are indicated.

Acknowledgements

First and foremost, I would like to thank my supervisor, **Dr. Shrawan Kumar Mishra**, for his invaluable assistance, support, and ideas during my dissertation process. His close observation and interest in my work over the last five years seem to have left a lasting impression on me. He provided me with an independent research environment yet provided support and suggestions in the time of need; I sincerely hope to continue learning from him. His attentive and enthusiastic approach to magnetism and magnetic transition characterization cannot be sufficiently conveyed in words, and I will be forever thankful to him. I would like to acknowledge my indebtedness to **Quantum Lab** lead by Dr. Shrawan Kumar Mishra and of course, other group members Dr. Shyam Babu, Rajnandini, Pawan, Nidhi, and Nitipriya. I am also thankful to my juniors Shantanu, Rohit raj, Akash, Navaneeth, and Mrigank for motivating me.

I'd like to thank the other members of RPEC, **Dr. B. N. Pal** of the School of Materials Science and Technology and **Dr. P. K. Roy** of the Department of Ceramic Engineering, for their insightful insights and support, which inspired me to widen my research interests. I'd like to thank **Prof. S. Ram** from IIT KGP for his ideas and scientific discussions that helped me increase my understanding.

I would also like to express my gratitude towards the faculty members of the School of Materials Science and Technology, **Prof. D. Pandey, Prof. R. Prakash, Prof. P. Maiti, Dr. (Mrs) C. Rath, Dr. A. K. Singh (Coordinator), Dr. C. Upadhyay, Dr. A. K. Mishra, Dr. S. Singh, and Dr. Nikhil (DPGC convener), Dr. Ravi Panwar, Dr. S. R. Singh, Prof. J. Kumar** for providing constant encouragement and invaluable suggestions during my Ph.D. work which greatly helped me to complete my work with confidence.

I would like to thank **Apoorv, Deepsovan, Aabhas, Dr. Amit, Mayank, Purnima, Harish, Rajesh, and Dr. Vishwas** for always being there for me in good times and bad. I am grateful to all of my friends for their encouragement and for sharing their unique experiences with me during my career. Furthermore, remember to thank Dr. Arun, Dr. Keshav, Dr. Priyanka, Dr. Deepshika, Dr. Dipti, Dr. Gaurav, Dr. Aniruddha, and Dr. Aravintha for their scientific and moral support. I truly enjoyed the company of juniors and batchments Taranga, Akhilesh, Sanjana, and Utkarsh at SMST.

I am also very thankful to technical and non-technical staff of my school: Mr. Amarnath, Ankit Jain, Ashwini, Sitaram Tiwari, Samir Dubey, Mahendra, Dharmendra, Waris, Awnish, Sudhakar, Dinesh, Rohan, Sajjan and Jaislaal for the cooperation and help. I specially acknowledged the support of the SMST and CIF (Central Instrumental Facility), IIT

BHU, Varanasi, and all staff, who have worked day and night to make this thesis research successful.

I would like to acknowledge Dr. Vasant Sathe from UGC DAE, Indore for providing Raman spectroscopy facility. I also like to thank Vivekanand Shukla and Thomas Brumme from Technical University Dresden, Germany, for DFT calculation and theoretical calculations.

I would like to convey my heartfelt thanks to my parents, **Shri Pursotam and Smt. Rekha Hissariya**, for their consistent encouragement, spiritual support, and blessing at every stage of my life. My heartfelt gratitude goes to my better half **Reetu**, whose encouragement and support over the last few years have made it all worthwhile. Her tolerance, kindness, and love have provided me with full balance and happiness despite the ups and downs. My heartfelt thanks for their love and care to my younger sister **Ms. Jyoti, Ms. Deepika, Ms. Pari, Ms. Hetal, Ms. Varsha**, and brother **Mr. Mukesh, Mr. Girdhar, Mr. Keshav, and Mr. Krishnam**. Their thoughts and prayers are with me at all times. Last but not the least, I am grateful to my daughter (**DIVA**), whose smiles boost my spirits.

I appreciate the delicious food provided by mess maharaj and employees, especially Lal Babu maharaj. Finally, I want to express my gratitude to God for giving me the strength to successfully finish my thesis. I also thank **Pt. Madan Mohan Malviya ji** for providing us access to this lovely campus to enjoy the Ph.D. journey.

Thanks a million!

Abstract

Complex oxide materials have gained significant interest due to their emerging properties and exceptional applications such as superconductivity, near-room temperature ferromagnetic ordering, magnetodielectric, exchange bias, magnetocaloric, magnetoresistance, half metallicity, and solar cells. These properties are corroborated with distinct lattice, charge, spin, orbital ordering and phase transitions. Based on the atomic distributions, these complex oxides have multiple different structures such as perovskite, spinel, garnet, and pyrochlore. Perovskites (ABO_3) and double perovskites ($A_2BB'O_6$) can be differentiated on the basis of octahedral arrangement and the presence of two different B-site cations (B/B'). Double perovskites are a special class of doped perovskites with 50 % doping at the B-sites that theoretically doubles the unit cell in a regular periodic approach. The fascinating features of double perovskites are mostly due to the two different kinds of octahedral configurations that resulted in ordered and disordered phases. The ordering of octahedra may be possible in three different types: rock salt, layered, and columnar. Antisites disorder (ASD) and antiphase boundary (APB) are common types of structural disorder features in double perovskite materials that consist of two different B/B' -site cations, which modify the properties by altering B/B' -sites.

Among the family of double perovskites, the La_2NiMnO_6 (LNMO) compound has attracted significant interest due to its various underlying properties and applications. In the case of ordered LNMO compound, the reported ferromagnetism phase is explained through the Goodenough-Kanamori (GK) rule for 180° ferromagnetic superexchange interaction between multiple oxidation states of Ni/Mn cations. Ordered LNMO is a ferromagnetic semiconductor having $T_c = 280$ K with various distinct magnetic properties across T_c . On the other hand, partially disordered LNMO shows exceptional magnetodielectric coupling, magnetoresistance, and magnetocapacitance that strongly influence by competing $Ni^{2+}-O^{2-}-Mn^{4+}$ exchange interactions. LNMO also manifest the Griffith phase and additional low-temperature magnetic anomalies. The lower temperatures transition has been attributed to the combined influence of antisites disorders and $Ni^{3+}-O^{2-}-Mn^{3+}$ ferromagnetic ordering. The multiple oxidation states of B/B' give rise to competing ferromagnetic (FM) and antiferromagnetic (AFM) exchange interactions that stabilized a magnetic frustrated state below the critical temperature. Previous studies have shown changes in T_c by varying the degree of ASD and APB through doping at the A-site and modifying the synthesis procedure of double perovskites. Few earlier studies have also observed the exchange bias in LNMO mediated by APB formed by the accumulation of ASD.

Herein, this thesis explores the phase evolution and microstructural morphologies of LNMO polycrystalline compounds using the size effect on various crystallites. Magnetization variation with temperature M-T and applied external magnetic field M-H loops are utilized to investigate magnetic transitions caused by the presence of multiple exchange interactions and antisite disorders. X-ray photoelectron spectroscopy (XPS) is utilized to probe the charge transfers in the LNMO crystallites. The XPS investigation verifies the existence of various valence states of cations with Ni^{3+} and Mn^{3+} contributing significantly to the stabilization of secondary ferromagnetic transitions. The thesis also provide the details of the theoretical calculation of the saturation magnetization (M_s) assuming different possible valence states. The core-shell structures are explained using transmission electron microscopy (TEM). The magnetization relaxation dynamics of the spin-glass (SG) phase that are derived from coexisting FM and AFM exchange interactions are explained within the framework of the power law, Vogel-Fulcher law, and Cole-Cole formalism that determine the nature of spin relaxation.

The present thesis also attempts to address the interesting aspects of the influence of ASD and APB upon the A-sites doping. Sm-substitution influences the structural characteristics of bond angle and bond length as well as magnetization. Present thesis emphasized SG state, spin dynamics, and exchange bias effect in these oxide compounds. Measurements of the continuous successive M-H loop and field reversal magnetization further support the observation of exchange bias phenomena. The Raman spectra are used to understand how the degree of ASD and APB influence through Sm-doping. This thesis highlights various modelling techniques to examine the nature of the SG state and its properties. The addition of Sm transforms the SG state into a cluster glass (CG) state. The determination of the Mydosh parameter, magnetization decay, magnetic memory, and rejuvenation effects has been utilized to elaborate on the SG state characteristics. In the proximity of CG transition a modified g-value ranging from 2.050 to 2.037 were reported utilizing electron spin resonance (ESR) techniques. The line width of the ESR signals increases across the transition due to spin freezing that is further examined by temperature-dependent ac-magnetic susceptibilities $\chi(\omega, T)$. To illustrate the magnetic memory and dynamics properties, two different complementary methods, namely the droplet and hierarchical models, are employed. Arrot's plot and mean-field theory are used to describe the order of magnetic phase transitions in this thesis. The density functional theory (DFT) explains spin state density and supports the presence of antisites. The DFT reveals that the Sm position in the unit cell has limited effect on the characteristics and that the antisites identify the various spin configurations. In a broad way, this thesis focuses on the magnetic characteristics of various protocols and models-based analysis.

This thesis systematically highlights the synthesis of $\text{La}_{2-x}\text{Sm}_x\text{NiMnO}_6$ ($x = 0, 0.1, 0.2$) compounds through the *sol-gel* process using all aqueous precursors. The physical characteristics of $\text{La}_{2-x}\text{Sm}_x\text{NiMnO}_6$ were probed using X-ray diffraction (XRD), Raman spectroscopy, magnetization, and susceptibilities measurements. The impact of site substitution on intrinsic behaviours and magnetic properties has been studied. The experimental studies suggest that the structural phase stability of $\text{La}_{2-x}\text{Sm}_x\text{NiMnO}_6$ improves significantly with Sm proportion as evident from the transformation of the compound from a biphasic (monoclinic + rhombohedral) structure into an aphasic (monoclinic, space group: $\text{P2}_1/\text{n}$). Sm-addition mediates variation in exchange interactions and ordering of Ni^{2+} - O^{2-} - Mn^{4+} that further suppress (284 K \rightarrow 245 K) the T_c . Lower T_c and higher saturation magnetization (M_s) resulted from the reduced degree of antisites disorder. Along with T_c , a massive shift (45.5 K \rightarrow 72.9 K) in glass transition temperature is also reported. Field-cooled magnetization M-H loops confirm the evidence of exchange bias in Ni^{2+} - O^{2-} - Mn^{4+} that reduces (120 Oe \rightarrow 28 Oe) with Sm proportion. The measurements of temperature-dependent magnetization M-T curves and frequency-dependent ac-susceptibility $\chi(\omega, T)$ were utilized to characterize the antisites-driven SG phase, magnetization relaxation dynamics, magnetic memory, and rejuvenation effect. The phase stability, lower T_c , tuneable M_s , and exchange bias make $\text{La}_{2-x}\text{Sm}_x\text{NiMnO}_6$ a potential candidate for its applications in energy-efficient devices.

In contrast, the $\text{La}_{1.5}\text{Sm}_{0.5}\text{NiMnO}_6$ compound shows the presence of antisites disorder in double perovskites and manifests various intriguing properties like SG state, exchange bias, and memory effect. The results suggest that the compound crystallizes in a monoclinic ($\text{P2}_1/\text{n}$) structure. The oxidation state of Ni(Mn) cations induces competing ferromagnetic and antiferromagnetic exchange interactions that originate from a heterogeneous spin frustrated state, as evident from reported magnetic anomalies in temperature-dependent magnetization measurements. SG state is evolved that manifests a exchange bias phenomenon (153 Oe) below T_{SG} (65.1 K). The strength of the exchange bias is reduced after successive magnetization reversal cycles that are performed at 5 K. The reported magnetic training effect is explained within the frameworks of meta-stable magnetic disorder across frozen antiphase boundaries in the frustrated SG state. Measurements of frequency-dependent ac-susceptibility suggest critical slowing dynamics and memory effect in the proximity of T_{SG} , which is described using a critical slowing model resulting in relaxation exponent $z\nu = 1.99 \pm 0.04$ and $\tau_0 = 8.91 \times 10^{-7}$ s. Employing DFT calculations, we report the insulating ferromagnetic ground state of $\text{La}_{1.5}\text{Sm}_{0.5}\text{NiMnO}_6$ in the ordered phase where Ni (Mn) appears to be in a 2+ (4+) state. The presence of antisites disorder eventually results in lower magnetic moments per formula unit that is

well matched with experimental observations. Our findings provide a pathway to control the induced exchange bias by manipulating the degree of ASD in such heterogeneous systems that have potential applications in designing magnetic sensors. Sm is known to have excellent thermal and optical characteristics; in the future, it would be interesting to investigate the thermal and optical characteristics and influence on Sm addition in LNMO compound.

Table of contents

List of figures	xxi
List of tables	xxvii
List of Abbreviations	xxix
List of Symbols	xxxii
Preface	xxxiii
1 Introduction	1
1.1 Perovskite	1
1.2 Double Perovskite oxide	3
1.3 Distinction of perovskites and double perovskites	5
1.4 Magnetic interaction	6
1.4.1 Superexchange interaction	6
1.4.2 Double exchange interaction	8
1.4.3 Crystal field splitting	9
1.5 Magnetism in double perovskite	10
1.5.1 Ferromagnetic insulating nature	10
1.5.2 Antiferromagnetic insulating nature	11
1.5.3 Ferromagnetic metallic nature	11
1.5.4 Spin-glass nature	11
1.6 Frustration mediated phenomena in double perovskite	14
1.6.1 Exchange Bias	15
1.7 Literature survey and background of $\text{La}_2\text{NiMnO}_6$	16
1.7.1 Crystal structure	16
1.7.2 Magnetism	17

1.7.3	Impact of doping	18
1.8	Motivation	19
1.9	Objective of the present thesis	20
2	Synthesis and characterization techniques	21
2.1	Synthesis/Growth method	21
2.1.1	Solid-state synthesis route	22
2.1.2	Sol-gel synthesis route	24
2.2	Characterization techniques	25
2.2.1	X-ray diffraction	25
2.2.2	Scanning electron microscopy	27
2.2.3	Energy dispersive X-ray spectroscopy	29
2.2.4	Transmission electron microscopy	30
2.2.5	X-ray photoelectron spectroscopy	31
2.2.6	Raman spectroscopy	33
2.2.7	Electron paramagnetic resonance	35
2.2.8	Magnetic property measurement system (MPMS)	36
3	Spin-up conversion and magnetization dynamics in $\text{La}_2\text{NiMnO}_6$	41
3.1	Introduction	41
3.2	Results and discussion	43
3.2.1	Growth of small core-shell	43
3.2.2	Valence state determination	46
3.2.3	Magnetization study in small core-shell crystallites	50
3.2.4	Collective spin dynamics in core-shell crystallites	57
3.2.5	Spin dynamics	61
3.3	Conclusion	62
4	Site substitution driven antisite disorder in $\text{La}_2\text{NiMnO}_6$	65
4.1	Introduction	65
4.2	Results and discussion	66
4.2.1	Structural and surface morphology	66
4.2.2	Magnetic characterstics	70
4.2.3	Magnetic memory and rejuvenation	76
4.2.4	Raman Spectra	78
4.3	Conclusion	79

5	Spin-glass state and exchange bias effect in $\text{La}_{1.5}\text{Sm}_{0.5}\text{NiMnO}_6$	81
5.1	Introduction	81
5.2	Computational details	83
5.3	Results and discussion	84
5.3.1	Structural analysis	84
5.3.2	Valence state determination	85
5.3.3	Temperature driven magnetic transitions	87
5.3.4	Isothermal magnetization and critical analysis	90
5.3.5	Isothermal magnetization loop	91
5.3.6	Exchange bias and magnetic training effect	92
5.3.7	Spin-glass dynamics	97
5.3.8	Magnetic memory effect	99
5.3.9	Electronic structure	100
5.4	Conclusion	106
6	Conclusions and future plan	107
6.1	Overview	107
6.2	Results and conclusions	107
6.3	Future scope of the work	108
	References	111
	Appendix List of Publications	129
	Vita	131

List of figures

1.1	Cubic unit cell where dark yellow, blue and maroon balls show A & B cations, and O anions, respectively.	2
1.2	Three different ordered distribution of octahedra in DP such as (a) rocksalt, (b) columnar, and (c) layered, here blue and yellow colour represents the BO_6 and $\text{B}'\text{O}_6$ octahedra, respectively.	3
1.3	Possible combination of different charge valance cations A, B, and B' in double perovskite.	4
1.4	Octahedra disorder (a) antisites defects, (b) antiphase boundary (APB), where green and purple circle represents as an octahedra.	5
1.5	Different types of superexchange interactions, between filled, half filled, and vacant orbit.	7
1.6	Double exchange interaction mediated through oxygen ion.	8
1.7	Crystal field splitting and Jahn-Teller distortion in Mn^{3+} cations, arrow indicates the spin up (\uparrow) & down (\downarrow) configuration.	9
1.8	(a) Degeneracy for a triangular lattice, (b) possible ground state for degenerated triangular lattice.	12
1.9	(a) FC and ZFC of dc-susceptibility for CuMn alloy at 6 Oe field (Nagata <i>et al.</i> (1979)), (b) Real part of ac-susceptibility versus T for CuMn; inset expanded view of SG cusp near T_f (Mudler <i>et al.</i> (1981)).	13
2.1	Flow chart of solid-state synthesis route adopted for the synthesis of LNMO crystallites.	23
2.2	Flow chart of sol-gel synthesis route adopted for the synthesis of LNMO crystallites.	25
2.3	Schematic illustration of XRD and Bragg's law.	26
2.4	Schematic diagram of various outcomes of electron beam interacting with the specimen.	28
2.5	Schematic diagram of photoelectron or principle of XPS.	32

2.6	Illustrate elastic and inelastic scattering via energy band diagram.	34
2.7	Energy level diagram for two spin states as a function of applied field B.	35
3.1	Observed (points) and Rietveld refined (line) XRD peaks of LNMO (sample S ₃), their difference (blue line), a standard stick pattern (bottom), Inset shows the variation in intense peak.	44
3.2	SEM images of different shapes LNMO in (a) S ₁ , (b) S ₂ and (c) S ₃ samples.	45
3.3	Particle size distributions in (a) S ₁ , (b) S ₂ and (c) S ₃ samples determined from SEM images in Fig. 3.2, showing an average size of 1.02, 1.15 and 1.28 μm, respectively.	46
3.4	(a, b, c) HRTEM images of a core-shell LNMO zoomed at different scales (S ₃), showing lattice arrays varied (d) near edges (gradually displaced off positions of atoms projected in a model in the inset), (e) below edges.	47
3.5	(a, b) HRTEM images of LNMO (S ₁) and (c) (002) lattice arrays enclosed in a (112) surface (regions A and B) at an angle 45°, as zoomed in the insets (d, e). The (002) arrays are curled near edges C in an oval shape.	48
3.6	(a) XPS survey for sample S ₁ , inset show normalized intensity for Mn-2p, and charge transfer (b) O-1s, (c) Mn-2p, (d) Ni-2p overlapped with La-3d spectra for specimen crystallites S ₁	49
3.7	Magnetic hysteresis loops of LNMO samples S ₁ , S ₂ , and S ₃ at 5 K, exhibiting (a) a small H _c magnified in the (inset), with model spin-lattices in (b) a Ni ²⁺ → Mn ⁴⁺ electron-transfer, (c) an antisite Mn ⁴⁺ inclusion.	51
3.8	ZFC–FC thermomagnetic curves of LNMO samples S ₁ , S ₂ , and S ₃ over 5 - 200 K (at H = 100 Oe), exhibiting a sharp T _{c2} peak in the derivatives (right) of its value rising in an exchange-coupled core-shell structure.	54
3.9	Irreversibility in ZFC–FC curves of LNMO samples S ₁ , S ₂ , and S ₃ over 150 - 280 K (at H = 100 Oe), showing how T _{c1} and T _{c1} * peak values in the derivatives (right) fall down on decreasing an antisite disorder.	56
3.10	Magnetic hysteresis loops of LNMO samples S ₁ at different temperatures (10 K, 20 K, 50 K, 100 K, 150 K, 200 K, 300 K.)	57
3.11	Temperature dependence of (a) χ' _{ac} and (b) χ'' _{ac} of sample S ₁ measured at various frequencies 20 to 600 Hz (given in the inset) at an applied ac-drive field of 200 Oe. The inset panel shows an enlarged χ' _{ac} part across 100 K.	58
3.12	(a) ln(τ) versus ln(T _f /T _{SG} - 1) and 1/(T-T ₀) plots for sample S ₁ , wherein the solid line represents the least squares fit for critical power law and Vogel-Fulcher law.	59
3.13	Cole-Cole plot for the magnetic susceptibilities of the crystallites S ₁	60

3.14	(a, b, c) ESR spectra at 298 and (d, e, f) at 78 K for S_1 , S_2 , S_3 crystallites blue colour represent the raw data and green colour represent the fitted data.	62
4.1	(a) The XRD patterns of S_0 , (b) S_1 , and (c) S_2 along with Rietveld refinement where black circle, red-line, blue-line, and green spike represent the experimental data, refined fit, their difference, and indexed Bragg's peaks, respectively. (d & e) shows the relative comparison of $\text{La}_{2-x}\text{Sm}_x\text{NiMnO}_6$ (where $x = 0, 0.1, 0.2$) and peaks belonging to the rhombohedral phase for sample S_0 . (f) the local crystal structure of $\text{La}_{1.8}\text{Sm}_{0.2}\text{NiMnO}_6$ where NiO_6 and MnO_6 octahedra indicated by grey and purple colour, respectively. The symbol * across 30° indicates the presence of negligible secondary phases present in all samples.	67
4.2	(a, b, & c) FESEM micrograph of S_0 , S_1 and S_2 , respectively. (d, e, & f) distribution of La and Sm in S_0 , S_1 and S_2 , respectively.	69
4.3	(a) TEM micrograph of S_2 , (b) High-resolution images(HRTEM) micrograph of marked area (c) lattice images of a selected area.	71
4.4	(a) dc-magnetization variation with temperature in ZFC/FC mode with 100 Oe magnetic field for samples S_0 , S_1 , and S_2 . Inset is the plot for the dM/dT , (b) Isothermal magnetization measurement at 5 K under an applied magnetic field of +500 Oe for S_0 , S_1 , and S_2	72
4.5	Magnetization loops collected at 5 K. Before measurements the sample was field cooled from 300 K in the presence of the applied magnetic field of ± 500 Oe (blue, red lines), suggesting the evolution of exchange bias for S_0 , S_1 , and S_2 in panel a, b, and c, respectively. Black line in panel a represent for M-H loop in ZFC. Inset shows an enlarged view of the panel (a).	73
4.6	Real part of ac- susceptibility (χ') as a function of temperature for (a) S_0 , and (b) S_2 reported at various frequencies. Power law fitting of relaxation time (τ) as a function of temperature for samples (c) S_0 , (d) S_2	75
4.7	Thermoremanent magnetization (TRM) relaxation data recorded at 10 K for S_0 and S_1 . Before measurements, the samples were first field cooled from 300 K to 10 K under an applied magnetic field + 10 kOe.	76
4.8	Magnetic relaxation behaviour of sample S_0 recorded at 15 K with magnetic field 100 Oe for (a) ZFC and (b) FC protocols. The relaxation behaviour indicates that the characteristic curve for t_3 is an ongoing trend of the curve for cycle t_1 indicating a robust magnetic memory nature.	77

4.9	(a) Raman spectra of samples S_0 , S_1 , and S_2 at 300 K, (b) at 81 K, (c) shifting in the peak position of stroke (S) and antistroke (AS) peaks with Sm-concentration, (d) full width at half maxima (FWHM) shift of S and AS bands as a function of Sm-proportion.	79
5.1	Room-temperature XRD pattern of LSNMO where the black dot, red line, blue line, and green sticks represent the raw data, fitted data, difference, and Braggs position, respectively. Inset shows the polyhedral picture of the unit cell where the green/blue ball represents the La/Sm and light blue and brown octahedra denote NiO_6 and MnO_6	84
5.2	XPS spectra of O $1s$ (a), Mn $2p$ (b), Ni $2p$ (c), and Sm $3d$ (d).	86
5.3	(a) ZFC/FC magnetization curves recorded under an applied external magnetic field of 100 & 500 Oe, red colour represents ZFC, and purple colour represent FC, (b) dM/dT for dc magnetization in ZFC protocol at 500 Oe field value.	88
5.4	(a) M versus H of LSNMO between 227 K and 275 K (in 4 K steps), (b) Arrott plots of M^2 vs (H/M) at different temperatures around T_c	90
5.5	ZFC isothermal magnetization at 5 K, 100 K, 200 K, and 300 K. Left inset shows the variation of the coercive field with temperature, and the right inset shows pristine M-H loops at 5 K up to +50 kOe.	92
5.6	(a) M-H measured at 5 K after cooling the sample from 300 K under a magnetic field of +500 Oe (black curve), and -500 Oe (red curve), representing the presence of exchange bias. (b) M-H loop measured at 5 K ZFC and FC mode in the presence of different cooling fields (0, 500, 1000 Oe). Inset shows the enlarged view.	94
5.7	(a) The zoomed view of hysteresis loop at 5 K after 1000 Oe cooling field with thirteen continuous cycles (magnetic training effect for EB). (b) The number of loops (n) dependent of H_{EB} extracted from training at 5 K. The blue solid line represents the best fit using empirical power law and the purple solid line represents the best fit as proposed by Mishra <i>et al.</i> 2009.	95
5.8	(a) Real part of ac-susceptibility variation with the temperature at different frequencies 50, 100, 200, and 300 Hz. Inset show enlarge view of cusp shifting, (b) $\ln(\tau)$ versus $\ln(T/T_{SG} - 1)$ and $1/(T - T_{VF})$ plots for sample LSNMO, wherein the blue and orange solid line represents the best fit of Vogel-Fulcher and Power law, respectively.	98
5.9	Temperature-dependent FC magnetization data during memory measurement. (b) magnetic relaxation measurement at a different field and temperature and the black line represents the best fit using stretched exponent function.	100

-
- 5.10 Upper panel shows the spin-resolved total density of the pristine LNMO in the right column and LSNMO in the right column for the chemical ordered and ferromagnetic phase. It also shows the density projections on p -orbital of Oxygen atoms and La atoms in the right column; the left column also includes the contributions of the Sm atom. The bottom panels show the spin-polarized partial density of states for Ni_ t_{2g} , Ni_ e_g and Mn_ t_{2g} , Mn_ e_g respectively. The Fermi level in the DOS is set to 0 eV. 101
- 5.11 Schematic representation of different magnetic configurations in LSNMO. . . . 102
- 5.12 Schematics of Sm substituted LNMO in $2 \times 1 \times 1$ supercell. These configurations stand for the doping positions where 2 La atoms are replaced by the Sm atoms. The red colour balls stand for oxygen atoms; the silver colour shows the Ni atoms; the purple colour balls show Mn atoms. The light brown colour balls are La, and the pink colour shows the dopant Sm atoms. 103
- 5.13 Two-dimensional slice projection of $2 \times 1 \times 2$ supercell of LSNMO shows the antisite defects ordering. In the left panel (system A), the Ni and Mn sites are exchanged cooperatively, and in the right panel (system B), Ni and Mn sites are exchanged in different unit-cell positions. In both of these systems, there are four Mn and four Ni atoms occupy their correct sites, and the rest of the eight octahedral sites are occupied by an equal number of Mn_{Ni} (Mn atoms occupying Ni) or Ni_{Mn} (Ni atom occupy Mn sites) antisites results in 50 % of antisite mixing in the ordered phase. System A has a mutual exchange of Mn and Ni position in one sub-unit, whereas in system B, Ni and Mn atoms are exchanged from two different sub-unit in the supercell. 105

List of tables

1.1	Crystallographic data (crystal structure and lattice parameter) with different synthesis conditions.	17
3.1	Structural parameter of small core-shell LNMO crystallites.	43
3.2	Chemical valence state for LNMO crystallites.	50
3.3	Tailored spin-transitions and M_s , and H_c values of small core-shell LNMO crystallites.	55
3.4	ESR fitting parameter at 300 K and 80 K for LNMO crystallites. Symbol (*) represents the parameter related to g_1	63
4.1	Structural parameters obtained from Rietveld refinement for S_0 , S_1 , and S_2 samples.	68
4.2	Quantification of Samples S_0 , S_1 and S_2 by EDX after excluding oxygen.	70
4.3	Magnetic parameters of $\text{La}_{2-x}\text{Sm}_x\text{NiMnO}_6$ where ($x = 0, 0.1, 0.2$).	71
5.1	Room-temperature lattice parameter, bond length (Å), bond angle (°), and atomic position driven from Rietveld analysis of LSNMO XRD pattern.	85
5.2	Room-temperature XPS analysis for sample LSNMO.	87
5.3	Comparison of energies in FM configurations for $2 \times 1 \times 2$ supercell with various doping arrangements described in Fig. 5.13.	104
5.4	Comparison of energies in ASD phases in $2 \times 1 \times 2$ supercell for various magnetic phases configuration 1, 2, and 3 as described in the text. The energies are compared independently for system A and system B.	106

List of Abbreviations

DP	Double perovskite
LNMO	$\text{La}_2\text{NiMnO}_6$
LSNMO	$\text{La}_{2-x}\text{Sm}_x\text{NiMnO}_6$
XRD	X- ray Diffraction
ASD	Antisite Disorder
APB	Antiphase Boundary
JCPDS	Joint committee on powder diffraction standards
ICDD	International Centre for Diffraction Data
TEM	Transmission Electron Microscopy
HRTEM	High Resolution Transmission Electron Microscopy
SEM	Scanning Electron Microscopy
FESEM	Field Emission Scanning Electron Microscopy
ESR	Electron Spin Resonance
XPS	X-ray Photoelectron Spectroscopy
MPMS	Magnetic Property Measurement System
SQUID	Superconducting Quantum Interfaces Devices
VSM	Vibrating-Sample Magnetometer
FM	Ferromagnetic
AF	Antiferromagnetic
EDX	Energy Dispersive X-ray spectroscopy
FWHM	Full Width Half Maximum
BSC	Backscattering Coefficient

ac	Alternating Current
dc	Direct Current
ZFC	Zero Field Cooling
FC	Field Cooling
NN	Nearest Neighbour
NNN	Next Nearest Neighbour
EB	Exchange Bias
SG	Spin-glass
CG	Cluster glass
SPM	Superparamagnetic
TRM	Thermoremanent Magnetization
SOC	Spin-Orbital Coupling
DFT	Density Functional Theory

List of Symbols

S	Total spin angular momentum
β	Angle (Lattice Parameter)
θ	Bragg's angle
L	Total orbital angular momentum
J	Total angular momentum
μ	Magnetic permeability
μ_B	Bohr magneton
μ_{eff}	Effective magnetic moment
H	Magnetic field intensity
H_c	Coercivity
M	Magnetization
M_r	Remanent magnetization
T	Temperature
H_{EB}	Strength of exchange bias
χ	Magnetic susceptibility
χ_{dc}	dc magnetic susceptibility
χ_{ac}	ac magnetic susceptibility
χ''	The imaginary part of magnetic susceptibility
χ'	The real part of magnetic susceptibility
μ_0	The magnetic permeability of free space
T_{SG}	Spin glass transition temperature
T_c	Curie temperature

T_f	Freezing temperature
τ	Relaxation time
θ_p	Curie-Weiss temperature
Ω	Mydosh parameter
ω	Ac frequency
ΔX	Peak to peak line width
X_{RES}	Resonance field
c	Speed of light
λ	Wavelength
θ_i	Incidence or local incidence angle
r	Ionic radii
K	Kelvin
(hkl)	Miller index
d	Lattice spacing
a, b, c	Lattice parameters

Preface

Complex oxide materials have attracted immense interest due to their exceptional characteristics and applications such as superconductivity, magnetoresistance, magnetodielectric, and electronic properties. These characteristics are related to structure, charge, spin, orbital ordering, and transitions. These complex oxides have various structures based on their atomic distribution and arrangement such as perovskites, spinel, garnet, and pyrochlore. Perovskites and double perovskites can be distinguished by their octahedral organization and the presence of two distinct B(B')-site cations. Double perovskite is a kind of doped perovskite with 50% doping at the B(B')-sites that theoretically doubles the unit cell in a regular periodic method. These two forms of octahedral configurations that generate ordered and disordered phases are important contributors to the interesting features of double perovskites. Octahedra can be ordered in three ways: rock salt, stacked, and columnar. ASD and APB are two frequent forms of disorders.

The LNMO compound has attracted significant interest in the family of double perovskites due to its multiple promising applications. Ferromagnetism in ordered LNMO is explained by the Goodenough-Kanamori rule for 180° ferromagnetic superexchange interactions. Ordered LNMO is a ferromagnetic semiconductor with $T_c = 280$ K, displaying various distinct magnetic properties across T_c . On another side, partially disordered LNMO shows exceptional magneto-dielectric coupling. Physical behaviours like magnetoresistance and magnetocapacitance in such compounds strongly depend on Ni^{2+} - O^{2-} - Mn^{4+} exchange interactions. Previous investigations suggest that different fascinating features and variations in Curie temperature by altering ASD and APB via doping at the A-site and modifying the synthesis procedure and conditions. Because of the underlying intrinsic strain, bi-phasic studies are more fascinating. In the case of thin film, a heterostructure is generated by an alternative layer of LaNiO_3 and LaMnO_3 and discovered charge transfer at the bilayer interface. There are very less reports on exchange bias in LNMO explained by APB formed by the accumulation of ASD. This thesis is divided into various chapters that are described below.

Chapter 1 presents a literature review about double perovskite, especially LNMO due to its useful properties and characterizations. This chapter explains the difference between perovskite & double perovskites and list out the major advantages of double perovskites. An overview of the synthesis process and doping affects the cation ordering and disordering, which affects the properties of double perovskite. The literature review about the different possible structures of LNMO with varying synthesis routes and conditions is also explained.

Chapter 2 describes the synthesis process used to prepare the LNMO nanocrystallites. As the literature implies that structure changes with synthesis conditions, we used two alternative ways namely the solid-state and sol-gel approaches to synthesize LNMO crystallites. The discussion of surface topology by SEM & TEM, and magnetization measurement techniques using a SQUID, MPMS in a distinct protocol. X-ray diffraction and Raman spectra corroborate the structural phase. The presence of multiple valences is identified by X-ray photoelectron spectroscopy. The electron spin resonance implies the resonance field and Lande g-factor.

Chapter 3 of the present thesis briefly investigates the phase development and microstructural study of LNMO using several synthesis techniques. The impact of millings on the microstructure and surface morphology of various lattice planes and crystallites. M-T curves and M-H loops are used to probe the various magnetic anomalies across T_c caused by multiple spin ordering. X-ray photoelectron spectroscopy (XPS) explains charge transfers found in nanocrystallites. The XPS investigation verifies the occurrence of various valance states of charge cations, with Ni^{3+} and Mn^{3+} contributing significantly to the stabilization of secondary ferromagnetic transitions. The thesis also deals with the theoretical calculation of the saturation magnetization assuming different possible valance states and comparing it with experiment data. The core-shell structures are imaged using TEM. The relaxation dynamics are explained by a power law, Vogel-Fulcher law, and also Cole-Cole formalism defines the nature of spin relaxation. The saturation magnetization assumes different possible valance states and compares.

Chapter 4 deals with the influence of ASD and APB on magnetic properties. Because of its premixture magnetic band structure, high spin-orbital coupling (SOC), and other properties, Sm is employed for doping at A-site. This chapter describes the Sm doping in $La_{2-x}Sm_xNiMnO_6$ (where $x = 0, 0.1, 0.2$) and their structure, size and shape, Raman spectroscopy, and magnetic properties. Sm doping has an effect on structural characteristics that is confirmed by the Rietveld refinement. Sm doping alters the biphasic (monoclinic + rhombohedral) structure into the aphasic monoclinic phase. The surface morphology analysis confirms particles are agglomerated and cations distributed homogenous and quantification within the nominal fraction. Our thesis primarily concerned with magnetic

characteristics. This thesis is concerned with spin glass dynamics and exchange bias. The SG state confirms with frequency-dependent cusp shift and power law fitting. The SG state nature further characterizes by the hierarchical modeling and magnetization decay measurement. The exchange bias confirms by the field reversal field cooling M-H loop measurement. The Raman spectra also illustrate how ASD and APB interact with Sm doping. The chapter has a brief discussion about antisites disorder with varying the properties such as exchange bias magnetic memory effect.

Chapter 5 highlights the synthesis and magnetic properties of $\text{La}_{1.5}\text{Sm}_{0.5}\text{NiMnO}_6$ crystallites. An increase in the Sm doping fraction transforms the typical spin glass into a cluster glass. The Mydosh parameter, magnetization decay, and memory and rejuvenation all explain the spin glass properties. To illustrate the dynamics, and Arrot's plot & mean field theory are used to describe the order of magnetic phase transitions in this thesis. The exchange bias confirms different field hysteresis loop measurements and magnetic training effects. The density functional theory (DFT) explains spin state density and supports the presence of antisites. The DFT reveals that the Sm position in the unit cell has little or no effect on the properties via consider different positions Sm atom in the unit cell. The antisites disorder are also confirmed by considering various spin configurations and antisites positions to analyse saturation magnetization.

Chapter 6 concludes the thesis with the novel findings. In a broad way, this thesis focuses on the magnetic characteristics of various protocols and models-based analysis. In this chapter, concluding remarks are presented on the basis of the experimental results and theoretical interpretation obtained in all the nano crystallite samples that are addressed in the thesis.

Chapter 7 describes the summary and conclusion of this work and also provides suggestions for the future prospect of current studies. The system with SG state and an exchange bias caused by ASD. Because Sm has good thermal and optical qualities, there is room to investigate the thermal and optical features.